Hindawi
Journal of Materials
Volume 2018, Article ID 1593947, 13 pages
https://doi.org/10.1155/2018/1593947

Research Article

Visible Light Assisted Photocatalytic Degradation of Chromium (VI) by Using Nanoporous Fe_2O_3

Abhilash Mavinakere Ramesh [1] **and Srikantaswamy Shivanna** [1,2]

[1] *Department of Studies in Environmental Science, University of Mysore, Manasagangotri, Mysore 570006, India*
[2] *Centre for Materials Science and Technology, Vijnana Bhavan, University of Mysore, Manasagangotri, Mysore 570006, India*

Correspondence should be addressed to Srikantaswamy Shivanna; srikantas@hotmail.com

Received 14 February 2018; Accepted 19 June 2018; Published 2 September 2018

Academic Editor: Sun-Jae Kim

A Fe_2O_3 nanoporous structure was prepared by using hydrothermal route; its physicochemical properties were effectively characterized using XRF, BET, FT-IR, VSM, SEM and EDX, DLS, XRD, and PL techniques. The surface area of the magnetic nanoporous structure Fe_2O_3 was higher than the normally synthesized Fe_2O_3 nanoparticle. The outcome of the photocatalytic removal of the chromium (VI) below the visible light irradiation confirmed that 82.11% of Cr(VI) was degraded by the Fe_2O_3 nanomaterials at 120 min of irradiation time. The improved photocatalytic activity of the nanoparticle was ascribed to efficient electron-hole separation. Fe_2O_3 was set up to be a tough and constant photocatalyst throughout recycling experiments. The conceivable mechanism for the electron-hole separation process on the heterojunction was probable. The synthesized samples own low band gap energy and a hollow structure appropriate for the improved photocatalytic activity. The toxicity of the samples was measured by using *Mus musculus* skin melanoma cells (B16-F10 (ATCC®, CRL-6475TM) which are set up to be safe for human cells; as a result, this systematic approach provides a better alternative upconversion material for integral photoabsorption.

1. Introduction

The pollution of unsafe metals is rising with widespread of industrial expansion [1]. Living point of view the metal chromium arises from its outstanding role in pollution in the form of industry and its toxicity to plants, animals, and microbes [2]. The vast amount of chromium is introduced into the surroundings throughout various sources like dyeing in fabric industries, compound manufacture, leather built-up, and metal plating which affect living organisms and cells [3, 4]. Chromium is in two oxidation states, Cr (III) and Cr (VI) hexa-valent, which is 600 times more toxic than the trivalent form in systematic manner [5, 6]. Several investigations have revealed that bulky sum of chromium (VI) is considered to be necessary for usual metabolic process [7]. The release into the sewage system causes a solemn environmental collision and chromium occurs mainly in Cr(III) form, which is oxidized into chromium (VI) due to the occurrence of organic compounds [8]. The ceiling stage of Cr (VI) tolerable in wastewater is 0.05 mg L^{-1} [9]. However, the superior levels of chromium metals have been found to be toxic to the internal organs [10, 11]. World health organization (WHO) has evidently stated that chromium (VI) is carcinogenic [9]. The human toxicity includes lung cancer and liver and gastric spoil [12]. Nowadays, the majority of the industries are facing the tricky problem of discarding of chromium (VI) in wastewater produced in huge quantity. Hexavalent chromium form chromate (CrO_4^{-2}) is considerably more soluble in water than trivalent chromium Cr(III) [13]. The chromium elimination treatment includes adsorption process, ion exchange, precipitation, reverse osmosis, and photocatalysis [14]. Most of these methods require high capital and recuring expenses and, therefore, they are not suitable for small-scale industries [15, 16]. Photocatalysis has been attracting growing interest because it provides a new, promising way to meet the environmental challenges of energy and sustainability; semiconductor photocatalysis has conventional much attention because of its high efficiency

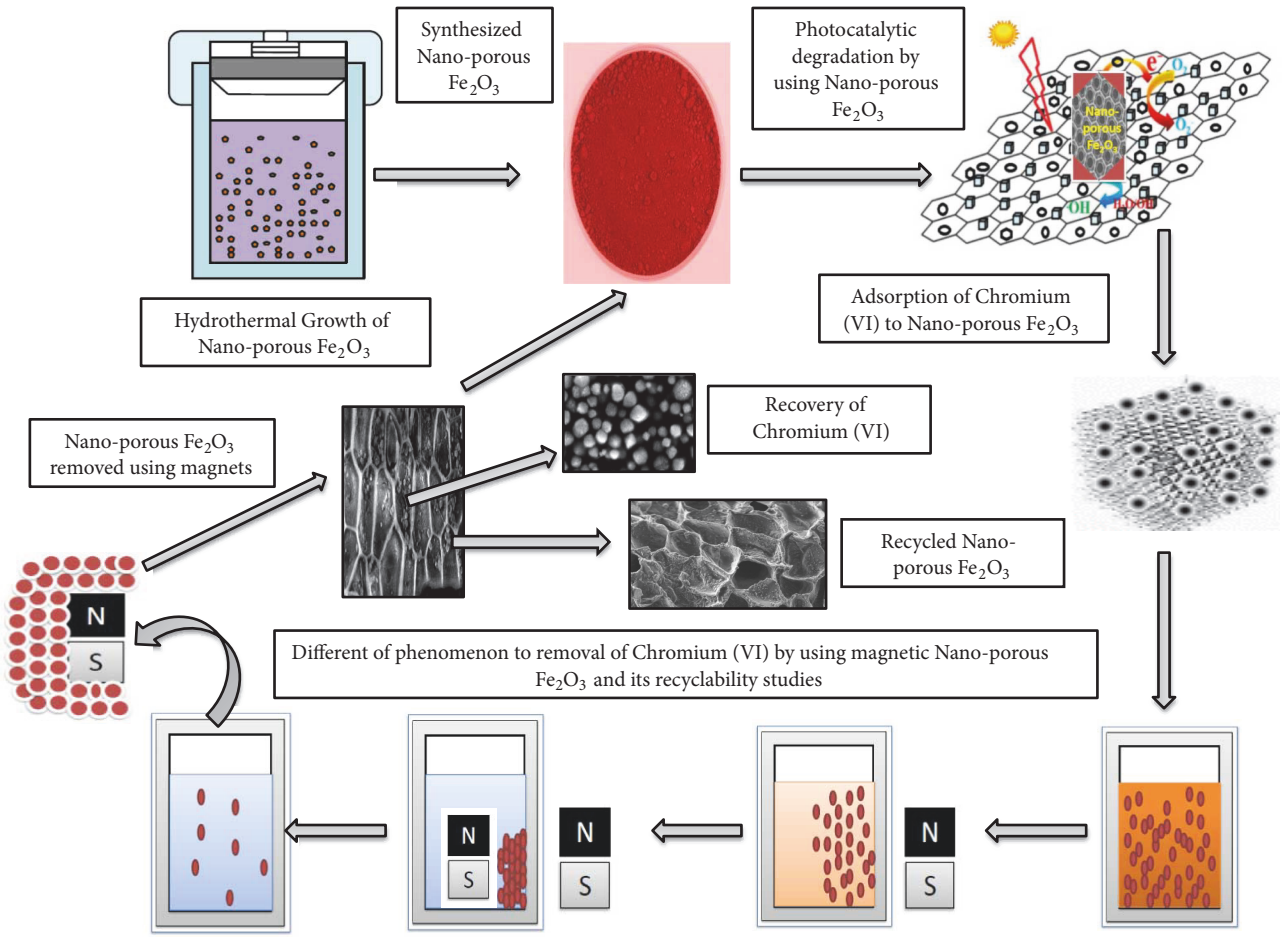

Scheme 1: Different phenomenon involved in removal of chromium (VI) by using magnetic nanoporous Fe_2O_3.

without inferior pollution [17]. In recent advances in efficient photocatalytic systems, the synthesis of high-performance photocatalysts with good recyclability is the one of the most important purposes; deplorably, the broad band gap of metal oxides confines the reasonable maintenance under visible light [18]. Moreover, the recovery of photocatalysts requires tedious steps during recycling. Therefore, recent research works have focused on developing magnetically separable visible light responsive photocatalysts to carefully use sunlight [19, 20]. Most of the researchers used Fe_2O_3 as a magnetic core of the nanoparticle for effective efficiency and utilization [21, 22]. Hydrothermal methods were usually used to prepare nanoderivatives so as to effectively be utilized for visible light-driven activity [23]. The systematic photocatalytic removal of Cr(VI) from wastewater is by using emerging materials in the batch progression experiments (Figure 19). The chromium was removed using photocatalyst with UV light and in the gloomy at diverse pH range. The utmost removal of Cr(VI) was pragmatic in pH 2 and TiO_2 showed peak ability for Cr(VI) removal than TiO_2 thin film [24]. To the best of our knowledge, there are no reports on the structured nanoporous facile Fe_2O_3 and its impact on the photocatalytic degradation of chromium (VI) under visible light. In the present study, we have effectively synthesized magnetic Fe_2O_3 from hydrothermal method in the deficiency of any capping agents. The physical properties such as morphology, element analysis, and surface area of the nanoporous have been studied in detail, and toxicity of the samples was measured using *Mus musculus* skin melanoma cells to clear determination of toxicity of the synthesized nanomaterial with an appraisal for the degradation of Cr(VI) in systematic manner under visible light irradiation to be compared with different emerging materials in this paper (Scheme 1). Therefore, this organized approach provides a better option upconversion material for fundamental photoabsorption. Moreover, the stability and durability of the Fe_2O_3 have also been studied *via* recycling experiments.

2. Material and Methods

2.1. Chemicals. Ferrous sulfate heptahydrate (99+%, Sigma Aldrich), ferric sulfate hydrate (97%, Fe 21.6%, Sigma Aldrich), ammonium hydroxide solution (28–30%, Sigma Aldrich), hydrochloric acid (37%, Fisher Scientific), and methanol (ACS reagent, Fisher Scientific) were used without any further purification. Ferrous chloride tetrahydrate ($FeCl_2.4H_2O$ Merck>99%), ferric chloride hexahydrate ($FeCl_3.6H_2O$ Merck>99%), salts, and ammonium hydroxide

(NH_4OH Merck, 25% of ammonia) were used for the synthesis of iron oxide nanoparticles. Chemicals were of reagent grade and used without further purification; deionized water was purified by a Barnstead/Synbron Nanopure-II purification system.

2.2. Hydrothermal Preparation of Nanoporous Fe_2O_3. The nanoporous Fe_2O_3 were synthesized using hydrothermal method. $FeCl_3$ and NaOH, ammonia (Aldrich, India), 10.14 g (37.5 mol) $FeCl_3.6H_2O$, and 7.45 g (37.5 mmol) $FeCl_2.4H_2O$ were dissolved into 25 ml of distilled water. Twenty-five milliliters of twenty-five percent ammonia was added to the salt solution under stirring condition at 700 rpm for 2 min right after 15 ml of mixture was put into a Teflon-lined stainless Morey autoclave, and the autoclave is heated to 180°C in an oven and maintained at 12 h reaction time. Temperature plays a vital role in the formation of well-defined spherical product. Autoclave was naturally cooled to room temperature, and the precipitates were washed with distilled water and isolated under magnet. The final products were dried at 60°C and were ready for characterization.

$$\mathbf{2FeCl_3.6H_2O + 2FeCl_2.4H_2O + 10NH_4OH} \longrightarrow \mathbf{2Fe_2O_3 + 10NH_4Cl + 24H_2O + H_2} \uparrow \quad (1)$$

2.3. Characterizations and Measurements. Magnetic measurement was accomplished using a vibration sample magnetometer (VSM, ADE EV9 Model). Brunauer-Emmett-Teller (BET) precise exterior area, aperture volume, and aperture size allocation of the samples determined by N_2 adsorption at 77 K by a Micromeritics ASAP, 2020, physico-adsorption analyzer. XRF band was recorded by Minipal- 4 benchtop model, with fine focus X-ray tube, MO target of multilayer monochromator of 17.5KeV for efficient elemental study. Ultima III Series, RIGAKU, TSX System, Japan, with Cu radiation (wavelength 1.54°A) at room temperature was used for wide-angle X-ray diffraction (XRD) patterns of the Fe_2O_3 recyclability studies. Scanning electron microscopic (SEM) images of the Fe_2O_3 was captured by HITACHI (S-3400 N, Japan) with 10 kV acceleration voltages. The Fe_2O_3 was measured using UV–Vis Spectrophotometer. The spectral analysis of Fe_2O_3 was carried out by measuring the optical density (OD) using Beckman Coulter, (DU739, Germany) scanning UV-Vis Spectrophotometer operated at a resolution of 1 nm between 280 and 800 nm. The Energy Dispersive Spectroscopy (EDS) analysis was carried out using HITACHI (Noran System-7, USA) system close to SEM for the finding of composite nanoparticles. The particle size distribution (PDS) and zeta capacity of iron oxide nanoparticle were observed with Microtrac (USA) element size monitor. The analyzer gives the size dimension and verification of particle size distribution. The concentration of profound metals in waste water is calculated with Inductively Coupled Plasma Atomic Emission Spectroscopy techniques (ICP-AES) using the Perkin-Elmer Optima 8000, ICP-OES; photocatalytic study was performed on a Heber-Immersion type photoreactor (HIPR-Compact, p-8/125/250/400) in an efficient manner and, finally, pH was observed by with an EU-TECH instrument pH meter. The electron-pore division development was confirmed by photoluminescence (PL) spectroscopy under an excitation wavelength of 325 nm.

2.4. Photocatalytic Study. The stock solution of Cr(VI) 1,000 ppm was equipped by dissolving K_2CrO_4 (A.R. grade); in the double-distilled water, batch studies were carried out using chromate stock solution to 1 L. The absorbance of chromate solution was calculated. The calibration curve of Cr(VI) was obtained at λmax = 540 nm. An identical particle size of the photocatalysts was among 120 to 500 μ size for photocatalytic dreadful conditions. In every study, an accurately weighted amount of Fe_2O_3 was used in 100 ml solution by maintaining pH of hexavalent chromium solution by means of adding of necessary amount of A.R. grade NaOH and HCl (E. Merck India) in the different flask at pH 2–7; the flask was sighted in Heber-Immersion type photoreactor, by steady shaking by magnetic stirrer. The photocatalyst is alienated from the solution by means of centrifugation. The removal efficiency of Cr(VI) was amplified through decline of pH from f 7 to 2. A highest exclusion was established to be high at pH 2, so pH was finalized at pH 2.

2.5. Photocatalysis of Industrial Effluent. The effluent containing Cr(VI) ions was taken away with diphenylcarbazide as masking agent creates the reddish purple color in the solution. The spectral study of Fe_2O_3 was performed by measuring the optical density (OD) by UV-Vis spectrophotometer operated at a resolution of 1 nm among 280 and 800 nm. The wastewater sample containing Cr(VI) was introduced with Heber-Immersion type photoreactor. In the test a precisely weighted quantity of photocatalysts was added in the flask, adjusting pH with NaOH and HCl in the different flask at pH 2 to 7. The flask was sited under Heber-Immersion type photoreactor, by steady shaking by magnetic stirrer. The photodegradation percentage was calculated by the following expression:

$$\%\ \text{Photo-degradation efficiency} = C_0 - \frac{C}{C_0} \times 100 \quad (2)$$

To authenticate the sorption of Cr(VI) over the Fe_2O_3 nanoporous material in the dark, the tests were carried out under identical conditions without visible light irradiation. The chemical oxygen demand (COD) was deliberate via dichromate oxidation method, subsequent to completion of photodegradation [25].

2.6. Cell Culture and Treatment. Cell culture and treatment of (B16-F10) cells were placed in tissue culture flasks and grown in Dulbecco's modified Eagle's medium (DMEM; Gibco, Thermo Fisher, USA), supplemented through 5% fetal bovine serum (FBS; Gibco, Thermo Fisher) and 1% antibiotic penicillin/streptomycin mixture (Santa Cruz Biotechnology, USA). The culture was maintained in a humidified atmosphere with 5% CO_2 at 37°C (Sanyo CO_2 Incubator; Sanyo, Japan). In the route of choosing the concentration

Table 1: X-ray fluorescence spectrum compound concentration.

Compound	Al-KA	Cl-KA	Cr-KA	Fe-KA	Cu-KA	Hg-LA	Pb-LA	Fr-MA1
Concentration (cps)	2.575	5163.511	439.862	19.643	45.822	45.763	17.247	3201.609

Table 2: Room temperature magnetic parameters of Fe_2O_3 nanoporous material.

Catalyst	Coercivity Hc (G)	Remanent magnetization Mr (emu g^{-1})	Saturation magnetization Ms (emu g^{-1})
Fe_2O_3	45.36	0.0489	0.5169

of Fe_2O_3, a dose-response curve with different concentrations (0.01, 0.05, 0.1, 0.5, 1.0, and 2.5μg/l) was plotted with explosion and MTT (2-(3,5-diphenyltetrazol-2-ium-2-yl)- 4,5-dimethyll-1,3-thiazole bromide) test, subsequent to 72 h of exposure. The concentrations of nanoporous Fe_2O_3 worn in the other experiments were 5, 50, 100, 200, 300, 400, and 500 μg/l for a time tie of 72 h; the studies were carried out in triplicate and three self-determining repetitions [26].

2.7. Statistical Analysis. Three replicates were analyzed for each experiment and by analysis of variance (ANOVA) using SPSS Inc. 16.0. Significant things of treatments were determined by F values ($p \leq 0.05$) and Tukey's HSD test.

3. Results and Discussion

The crystallinity and morphology of the synthesized nonporous materials were characterized by using XRF, SEM and DLS, and PL spectra analysis. The elements in the nanoporous were verified using EDX and elemental mapping analysis. The magnetic properties (coercivity (Hc), saturation magnetization (Ms), and remanent magnetization (Mr)) were studied via VSM analysis. The surface area and pore volume were calculated from the BET analysis. The photocatalytic activity was evaluated for Cr(VI) degradation under visible light irradiation. The electron-hole severance process in Fe_2O_3 was significantly supported by the PL analysis. The photochemical stability and reusability of Fe_2O_3 by using XRD was also discussed in detail in this article.

3.1. Characterization. X-ray fluorescence is recorded with fine focus X-ray tube, MO target of multilayer monochromator of 17.5KeV. The XRF spectra of Fe_2O_3 clearly indicate that the presence of Fe^{+3} XRF patterns of Fe_2O_3 nanoporous materials is shown in Figure 1.

The diffraction peaks in 6.2 to 7.2 keV and the concentration of the compound Fe-KA being 153256.1 (cps) are perfectly aligned to the cubic phase Fe_2O_3 and are shown in Table 1.

The diffraction peaks related to other inferior phases of iron oxide are not detected. The magnetic parameters such as coercivity, saturation magnetization, and remanent magnetization are shown in Table 2. The Ms value of the nanoporous material is much lower than the other photocatalytic materials. Material is supposed to be renowned that the magnetic

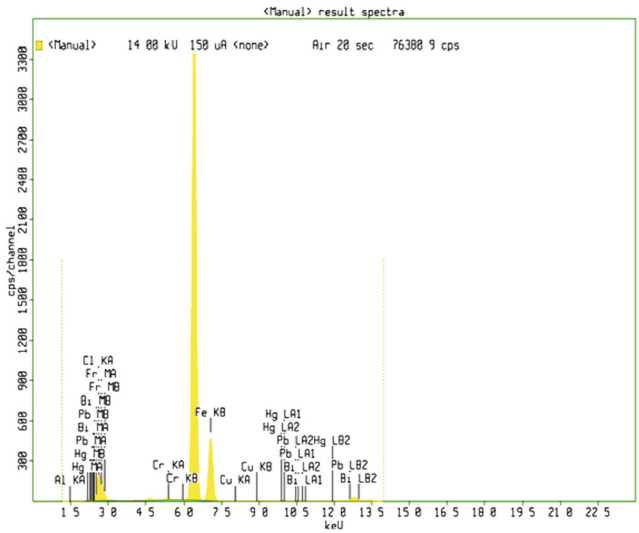

Figure 1: XRF spectra of Fe_2O_3 nanoporous material.

behavior (Mr) of Fe_2O_3 is still retained after photocatalytic procedure suggesting the suitability of the nanomaterials for magnetic separation and recovery [27, 28]. The decline in Mr for the nanoporous material not only reduces the aggregation of the catalyst but also enhances the reusability.

The nanoporous iron oxide control sample shows only an insignificant uptake at the squat relative pressure end (P/P0< 0.05) and a quick uptake with an H-3 type hysteresis loop at high relative pressure end (P/P0> 0.9), representing that the sample contains predominantly huge mesopores and/or macropores (average size: 28 nm). In this sample, the mesopores/macropores should be the inter-nanoparticle pores resulting from the aggregation of the crystalline Fe_2O_3 nanoparticles. The crystalline Fe_2O_3 nanoparticles in the iron oxide sample have an estimated average diameter of 16 nm, which is nearly identical to the average size estimated above significantly shows enhanced surface area (354 m^2g^{-1}) and pore volume (0.29 cm^3g^{-1}). Meanwhile, both surface area and pore volume show slight increases with the increase of the iron oxide pore. Surface area is an important parameter to determine the photocatalytic activity of nanoparticles and is performed by BET surface area analysis, shown in Table 3. A photocatalyst with a high surface area is likely to absorb more Cr(VI) and react more rapidly; N_2 adsorption-desorption isotherms of Fe_2O_3 are depicted. The isotherms of Fe_2O_3 are recognized as type-IV as per IUPAC classification, indicating the presence of mesopores [29]. Moreover, the isotherm profiles have H_2 (P/P0 from 0.4 to 0.9) and H-3 type (P/P0 from 0.9 to 1.0) hysteresis loops, signifying that there are slit-like pores [30]. The surface area and pore volume of the nanoparticle are lower than those of other photocatalytic

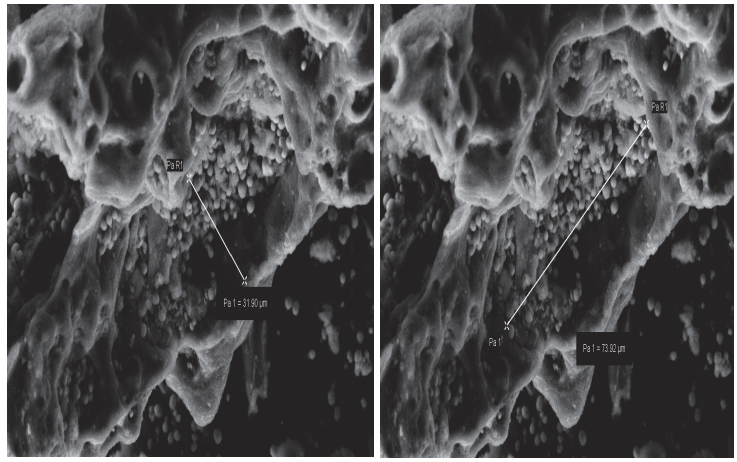

Figure 2: SEM images of Cr(VI) adsorbed on Fe_2O_3 surface.

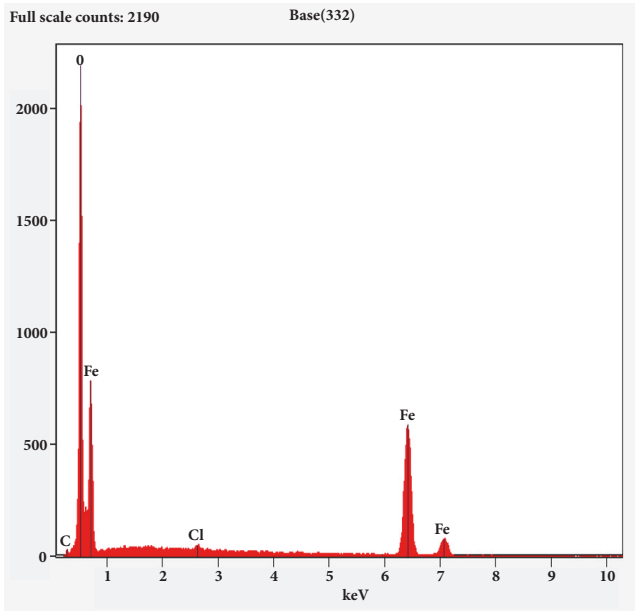

Figure 3: Energy dispersive X-ray analyzer result of Fe_2O_3.

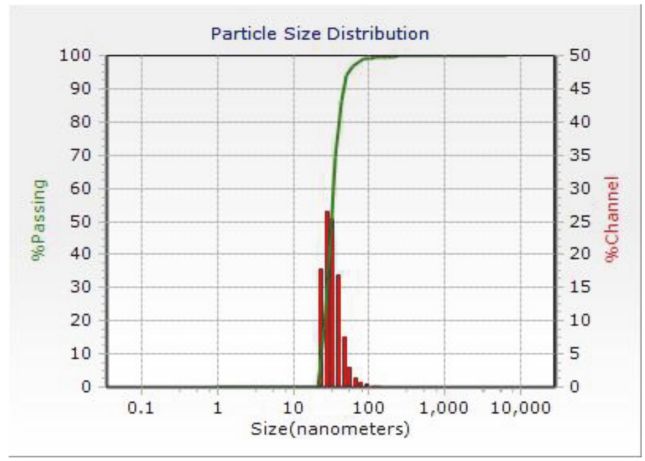

Figure 4: Dynamic light scattering/particle size distribution result of Fe_2O_3.

metals and, in general, surface area is not the crucial factor that determines the photocatalytic activity of silver based catalysts [31, 32].

In the present research, Fe_2O_3 nanoporous material clutches the structural and functional groups on the surface, potentially fastening the metals. A piece of iron oxide has a specific number of active coordination sites, depending explicitly on the surface area. Surface of the iron oxides can be very influential for the chance of the allied metal ions to bind to the surface via specific or nonspecific adsorption. Adsorption to iron oxide surface is pH-reliant and slight fluctuations in the pH may engage in recreation in controlling the adsorption-desorption reactions. The morphology of Fe_2O_3 was carried out by Scanning Electron Microscopy; SEM images were displayed in Figure 2. Fe_2O_3 is mainly composed of spongy like squared nanoporous and the particle length and breadth are 73.92μm and 31.90μm, respectively. However, all the nanoporous materials are closely packed and aggregated. EDX was carried out to examine the elemental composition of the synthesized photocatalysts and the results are shown in Figure 3. The peaks corresponding to Fe and O are clearly observed at their normal energy levels, showing the elemental composition, atomic percentage, and weight percentage of the photocatalysts. Consistent with the XRF results, EDX spectra confirm the purity of the prepared samples.

The histogram of dynamic light scattering analysis for particle size distribution of controllable composites is depicted in Figure 4. DLS analysis is regarded as one of the reliable techniques for evaluating particle size, distribution, and zeta potential of nanoparticles in solution. The present scrutiny revealed the presence of particles with an average diameter of 33.70 nm in the aqueous colloidal solution. The surface charge (zeta potential) of the Fe_2O_3 nanoporous plays a vital role during the interaction with other environmental degradation systems. The particles zeta potential value is

Table 3: Results from N_2 sorption characterization.

Sample	Surface area (m^2g^{-1})[a]					Pore volume ($cm^3\ g^{-1}$)[b]					Average meso-/macropore size (nm)[c]
	S_{BET}	$S_{d<20\,Å}$	$\%S_{d>20\,Å}$	$S_{d>20\,Å}$	$\%S_{d>20\,Å}$	V_{total}	$V_{d<20\,Å}$	$\%V_{d>20\,Å}$	$V_{d>20\,Å\ (des)}$	$\%V_{d>20\,Å}$	$D_{meso/macro}$
Nanoporous Fe_2O_3	354	31	11%	301	89%	0.29	0.02	7%	0.27	93%	7

[a]BET surface area (S_{BET}), surface area of micropores ($S_{d<20\,Å}$) and surface area of meso-/macropores ($S_{d>20\,Å}$) determined with the t-plot method. The percentage data denotes the percentage of surface area of micropores or meso- and macropores relative to the total surface area.

[b]Total pores volume (V_{total}), micro volume ($V_{d<20\,Å}$) determined with the t-plot method. The percentage data denote the percentage of pore volume of micropores relative to the total pore volume.

[c]Average meso-/macropores size ($D_{meso/macro}$) determined from the N_2 desorption data with NLDET model.

13.9 mV that was entirely determined in the present study. Nanoparticles with a zeta potential of −10 and + 10 mV have a neutral charge; when it is greater than +30 mV or less than −30 mV, it is considered to be strongly cationic and anionic, respectively. Based on the results, the growth mechanisms of the nanoporous Fe_2O_3 can be predicted.

In Figure 5, the peaks at 619 cm^{-1} were attributed to the Fe-O bond vibration of the Fe_2O_3. The spectrum showed the bands at 1390 cm^{-1} and 1130 cm^{-1} correspond to the out-of-level surface C–H vibration caused by the relic of triethylamine on the surface of particles and the peaks lying on around 1628.59 cm^{-1} were tentatively assigned to the vibration of C–N bond [33]. The peaks at 3149 cm^{-1} are assigned to the ν(N ± H) vibrations [34], and peaks at 3448 cm^{-1} were assigned to the O-H stretching vibration of absorbed water [35].

A predictable loom is working to estimate the band gap energy (Eg) values [36]. The band gap energy values of Fe_2O_3 nanoporous material were calculated to be 2.03 eV correspondingly.

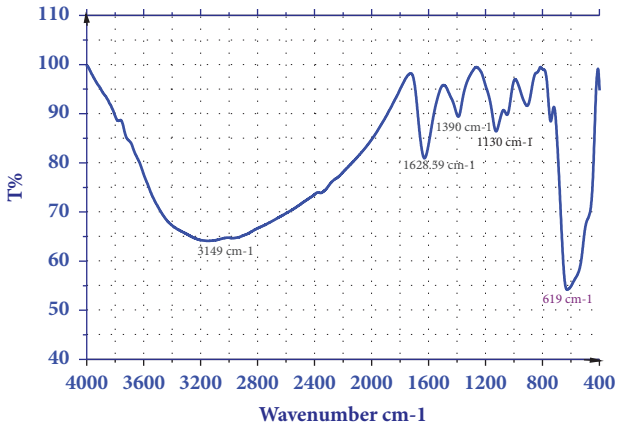

Figure 5: FT-IR spectrum of nanoporous Fe_2O_3.

3.2. Photocatalytic Activity. Sequentially to assess the photocatalytic activity of the geared-up samples under the visible light irradiation, the trials were conducted with an initial Cr(VI) concentration of 9 mM, catalyst concentration of 0.75 g/L^{-1}, and pH 5. The photocatalytic routine of Fe_2O_3 was shown in Figure 6.

pH is the imperative parameter that influences the photocatalytic activity [37]. Trials were performed at pH values of 3.0 (acidic), 5.0 (basel pH of Cr(VI)), and the 7.0 (neutral) and 9.0 (alkaline). The deliberation of heavy metal and catalyst dosage were fixed at 9 mM Cr(VI) and 0.75 g L^{-1} (Fe_2O_3), respectively. The outcome of pH on the photodegradation of Cr(VI) is revealed in Figure 6. The photodegradation percentage of Cr(VI) was found to be 60.24%, 82.12%, 65.17%, and 51.27% for pH 03, 05, 07, and 09 in that order. It is illustrious that the photocatalytic activity is decreased by the increase or decrease of Cr(VI) solution pH.

The photocatalytic activity of ZnO (viable, 99% purity by particle size 0.1–4.0 mM) and TiO_2 (marketable, TiO_2-P_{25}) was also willful for reference. The study confirmed that 81.11% of Cr(VI) was degraded by the Fe_2O_3 nanomaterials at 120 min of irradiation time. The degradation percentages

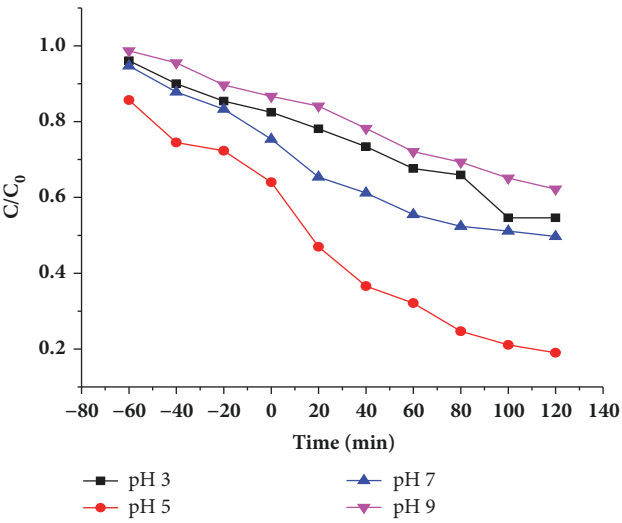

Figure 6: Role of pH on the photodegradation of Cr(VI) by Fe_2O_3 nanomaterials.

of TiO_2, ZnO, and CuO_2 are 56.31%, 69.92%, and 71.32%, respectively. The activity of Fe_2O_3 (96.11%) is superior when compared to the standards in Figure 7. This may be credited toward its photosensitizing ability.

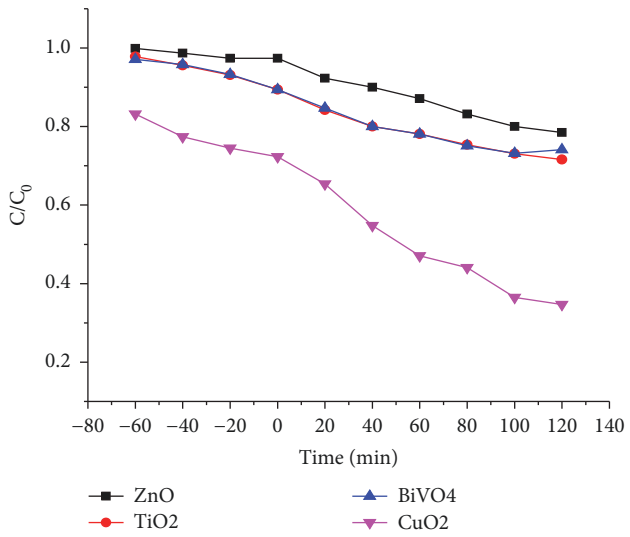

FIGURE 7: Photodegradation of Cr(VI) using various photocatalysts.

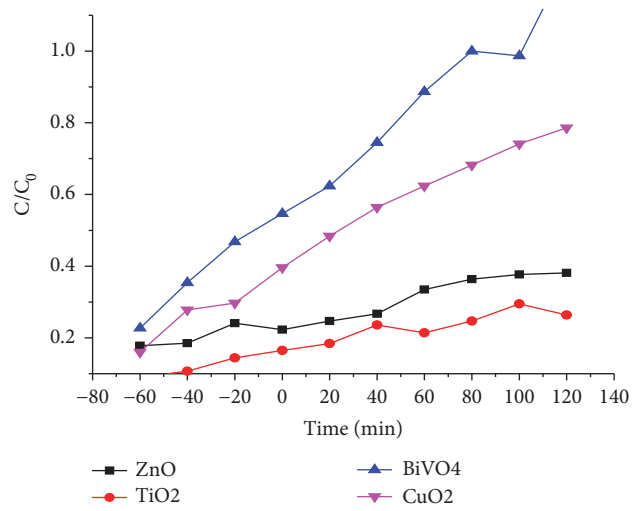

FIGURE 8: Kinetics of Cr(VI) photodegradation using different catalysts.

As per zero point charge (P_{zc}), the external property of Fe_2O_3 is pretentious by the logical change in pH. The values of Fe_2O_3 were found to be 7.3, respectively. It is appealing to mention that Cr(VI) is a toxic heavy metal. An acidic environment is helpful to increase the electrostatic lure between the proton from the catalyst and the toxic heavy metal and thus the photodegradation is high. At low pH (below 5), the odds for agglomeration are high, which will decrease the active surface area available for heavy metal adsorption and photon absorption. At finest pH, the predominant iron, namely, Fe $(OH)^{2+}$, not only forms Fe (II), the most important catalytic candidates in the photodegradation reactions, but also produces the further $^{-}$OH dependable for heavy metal [38]. pH was greater than p_{zc}; the exterior of Fe_2O_3 becomes negatively charged. Consequently, the negatively charged Cr(VI) molecules are repelled by the catalyst surface, and this leads to a decrease in the photocatalytic activity. The extremely alkaline conditions are favorable for the cohort of more number of less reactive high-valence iron species [33].

3.3. Photodegradation Kinetics of Cr(VI). The Langmuir-Hinshelwood model was effectively used to investigate the kinetics of Cr(VI) photodegradation. The photocatalytic experiments were carried out under optimum reaction conditions [Fe_2O_3= 0.75 g /L^{-1}, Cr(VI) = 9 mM and pH 5]. Figure 8 shows the logarithmic plot of Cr(VI) concentration as a function of irradiation time. The pseudo-first-order kinetics experiential rate constant for Fe_2O_3 is 1.21 × 10^{-2} s^{-1} is appreciably higher than of TiO_2 (4.36 ×10^{-3} s^{-1}) and CuO_2 (6.45 × 10^{-3} s^{-1}). Hence, the activity of the Fe_2O_3 nanoporous material is about 2.4 times higher than that of other verified material in systematic manner. Negligible photocatalytic activity was shown by ZnO (2.11 ×10^{-3} S^{-1}) in this research.

It is necessary to determine the degree of mineralization of Cr(VI) during photodegradation. Chemical oxygen demand (COD) is a fundamental investigation for assessing the superiority of effluents and wastewaters before release. It predicts the oxygen obligation of the effluent and is used to monitor and control discharges and to assess the treatment plant routine. The fraction change in COD during photodegradation was measured under optimum reaction conditions [Cr(VI) concentration 9 mM, catalyst concentration 0.75 g L^{-1}, pH 5, and irradiation time 180 min]. The solutions obtained after 180 min of photodegradation showed an important decrease in COD (59.52%); i.e., after 180 min COD was decreased from 89 mg L^{-1} to 36.14 mg L^{-1}. It has been observed that Cr(VI) molecules were to some extent degraded to intermediates, and small fraction was subjected to complete mineralization, persuading radical scavengers. To further gain insight into the degradation mechanism, the responsibility of the reactive species on the photocatalytic activity was determined using a series of scavengers. The experiments were carried out under optimum reaction conditions (Cr(VI) = 9 mM, Fe_2O_3 = 0.75 g L^{-1}, and irradiation time = 120 min) in the company of scavengers (2 mM for 200 mL heavy metal solution) such as t-BuOH for •OH [39], benzoquinone (BQ) for $O•^2$ [40], and potassium iodide (KI) for holes and •OH [41]. The effect of t-BuOH, BQ, and KI on the photodegradation proportion of Cr(VI) is shown in Figure 9. It is perceptibly observed that the photodegradation percentage of Cr(VI) is reduced to 36.79%, 39.75%, 49.69, and 74.11% after the addition of KI, t-BuOH BQ, and, Blank respectively. The photocatalytic activity of the nanoporous was surprisingly concealed in the presence of scavengers, indicating that both O^2• and the •OH are enthusiastically occupied in the photodegradation process.

3.4. Photocatalytic Mechanism. The valence band (VB) and the conduction band (CB) positions of Fe_2O_3 are expected by using the Butler and Ginley equation [42, 43].

$$E_{VB} = EVB = x - E^e + 0.5Eg \quad (3)$$

where x is the fixed electronegativity of the semiconductor, E^e is the energy of free electrons on the hydrogen scale (*ca.*

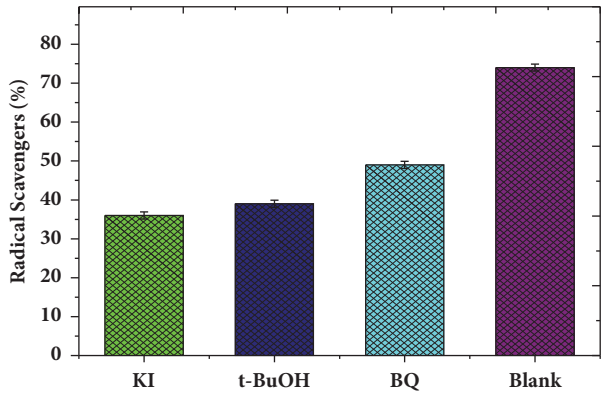

FIGURE 9: Role of different radical scavengers on the photodegradation of Cr(VI).

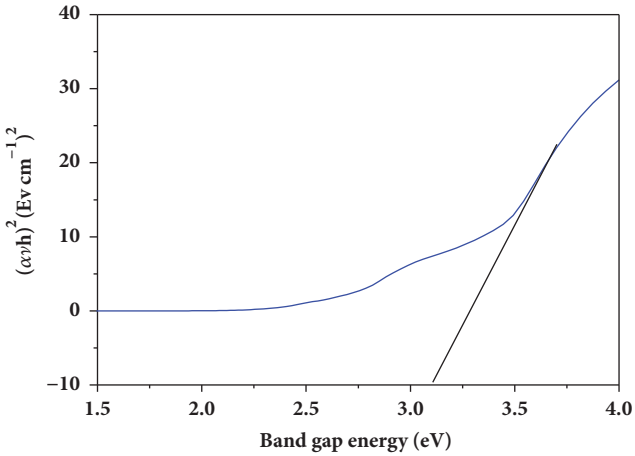

FIGURE 10: Tauc plot for the nanoporous Fe_2O_3.

4.5 eV), E_{VB} is the *VB* edge potential, and *Eg* is the band gap energy of the semiconductor. The CB position can be deduced using the following equation:

$$E_{CB} = E_{VB} - Eg \tag{4}$$

The x values of nanoporous Fe_2O_3 3.16, accordingly, the *VB* and *CB* of Fe_2O_3, were estimated to be 2.11and 0.23 eV, respectively. Through light irradiation, electrons and holes are produced in the *CB* and *VB* of Fe_2O_3. The photogenerated electrons can simply drift from the *CB* of nanoporous Fe_2O_3 under the action of a built-in electric field [44]. The holes will stay in the *VB* of Fe_2O_3. These progression forces successfully extend the duration of charge carriers at the Fe_2O_3 nanoporous face. The electrons accumulate on the *CB* of nanoporous Fe_2O_3 corresponding with dissolved oxygen to form a super oxide radical ($O^2\bullet$), and they additionally react with H^+ to acquiesce to the hydroxyl radical (•OH). The photogenerated holes on the *VB* of iron oxide can unswervingly oxidize the Cr(VI) or react with H_2O to produce hydroxyl radicals (·OH). The metal frame of the Cr(VI) compound is hurriedly tainted by the reactive species ($O^2\bullet$, •OH and h^+) generated in this photocatalytic process.

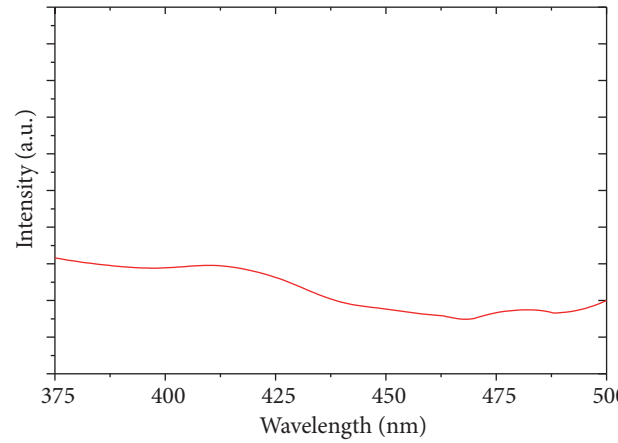

FIGURE 11: PL spectra of Fe_2O_3.

3.5. Tauc Relation for Finding Out the Band Gap. Tauc relation is the suitable tool and the appropriate technique to determine the optical absorption spectrum of a nanomaterial; the absorption coefficient α for material is given by

$$\alpha h\gamma = A\left(h\gamma - Eg\right)^n \tag{5}$$

The optical band gap was expected by plotting the straight line of $(\alpha h\gamma)^2$ v/s photon energy as shown in Figure 10. Bringing to a halt the tangent to the plot provides a good estimate of the band gap energy of nanoporous Fe_2O_3. The band gap of the hydrothermally synthesized nanoporous Fe_2O_3 was investigated that 3.16 eV. nanoporous Fe_2O_3 nanocomposite results in a remarkable increase in the photocatalytic activity of Cr(VI).

The electron-hole division method in Fe_2O_3 was additionally incorrigible by PL analysis. PL spectra of Fe_2O_3 are evidently shown in Figure 11. The PL emission peaks are observed at 416 nm and 440 nm [45, 46]. This is mostly accredited to the effectual separation of charge carriers on the marginal photocatalyst.

3.6. Reusability of Photocatalysts. In order to investigate the stability and durability of the Fe_2O_3 nanomaterial recycling experiments were conducted for the photodegradation of Cr(VI), after the successful recycling results of X-ray fluorescence were shown in Table 4. After the completion of each cycle, the photocatalyst was collected using an external magnet, washed with double-distilled water, dried overnight, and utilized. As depicted in Figures 12 and 13, the photodegradation percentages of Cr(VI) for five successive cycles were found to be 78.15%, 74.65%, 72.45%, 71.98%, and 70.24%, respectively; a photocatalyst is one of the most important supplies for unbeaten industrial applications. The Fe_2O_3 nonporous materials exhibit 76.24% of photocatalytic activity after five successive cycles in Figure 16 and, in Figures 14 and 15, the decrease in activity following two cycles is credited to the loss of catalyst throughout the easy washing process [47, 48]. In addition, there is no obvious change observed in the XRD pattern of Fe_2O_3 in Figure 17, after five cycles. These results indicate that the Fe_2O_3 nanoporous

Table 4: X-ray fluorescence spectrum compound concentration after successful recycling cycles.

Compound	Al-KA	Cl-KA	Cr-KA	Fe-KA	Cu-KA	Hg-LA	Pb-LA	Fr-MA1
Concentration (cps)	1.025	No-intensity	No-intensity	19.643	2.367	6.324	2.145	3.265

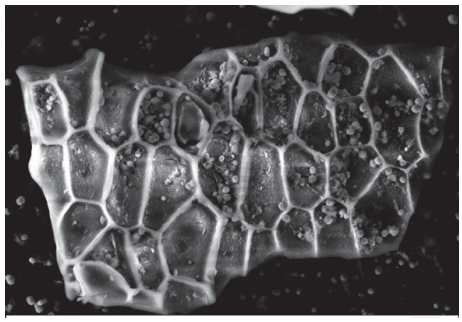

Figure 12: SEM (500 nm) scale image of Cr(VI) absorbed on the surface on nanoporous Fe_2O_3.

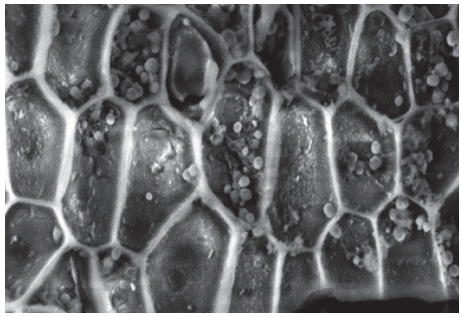

Figure 13: SEM (1 μm) scale image of Cr(VI) absorbed on the surface on nanoporous Fe_2O_3.

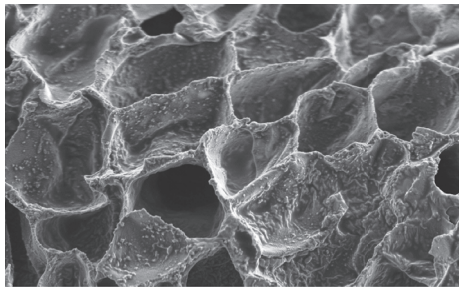

Figure 14: SEM (1 μm) scale image of nanoporous Fe_2O_3 after the recycle performance (c) recovered Cr(VI) Fe_2O_3 form for safe disposal.

materials could be used as a stable photocatalyst for the degradation of heavy metals in industrial wastewater under sunlight as clearly indicated in the XRF pattern, Figure 18.

3.7. Toxicity Test. The exceptional upconversion materials for emitting visible light are the suitable candidates for both i*n vivo* and *in vitro* bioimaging as well as in photodynamic therapy. In addition to photocatalytic activity, since the upconversion particles need to be used in living cells, the toxicity study is also very important. The outcome showed

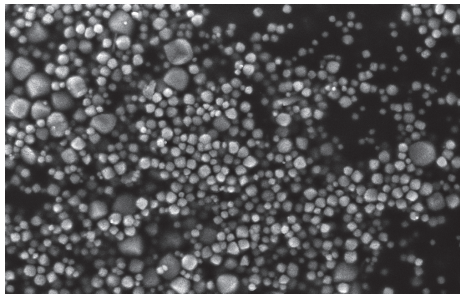

Figure 15: SEM (500 nm) scale image of recovered Cr(VI) Fe_2O_3 form for safe disposal.

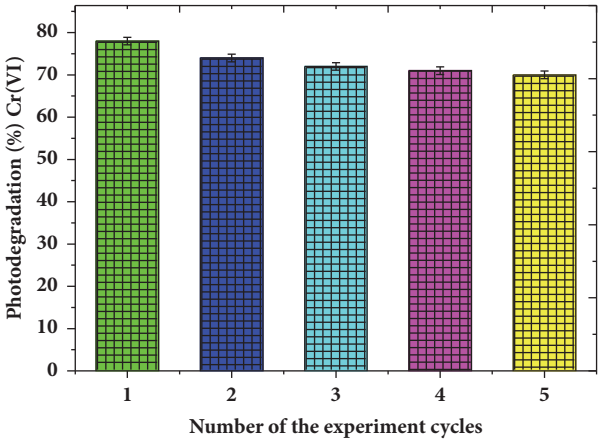

Figure 16: Recycling performance of Fe_2O_3 after the photodegradation of Cr(VI).

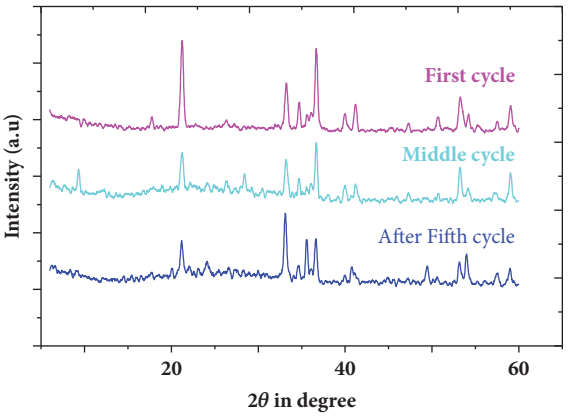

Figure 17: XRD patterns of Fe_2O_3 before and after successful cycles recycling.

that the assorted sample decreases the viability of B16-F10 cells in a dose-dependent manner as in Figure 20. As shown in 5 g/mL concentration, the lowest concentration of sample

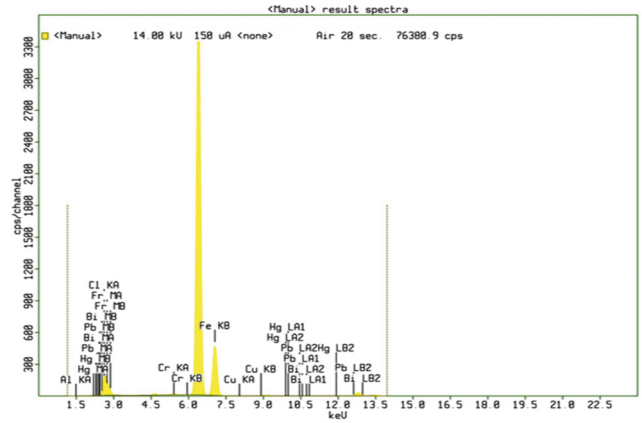

Figure 18: XRF spectra of Fe_2O_3 nanoporous material after successful recycling.

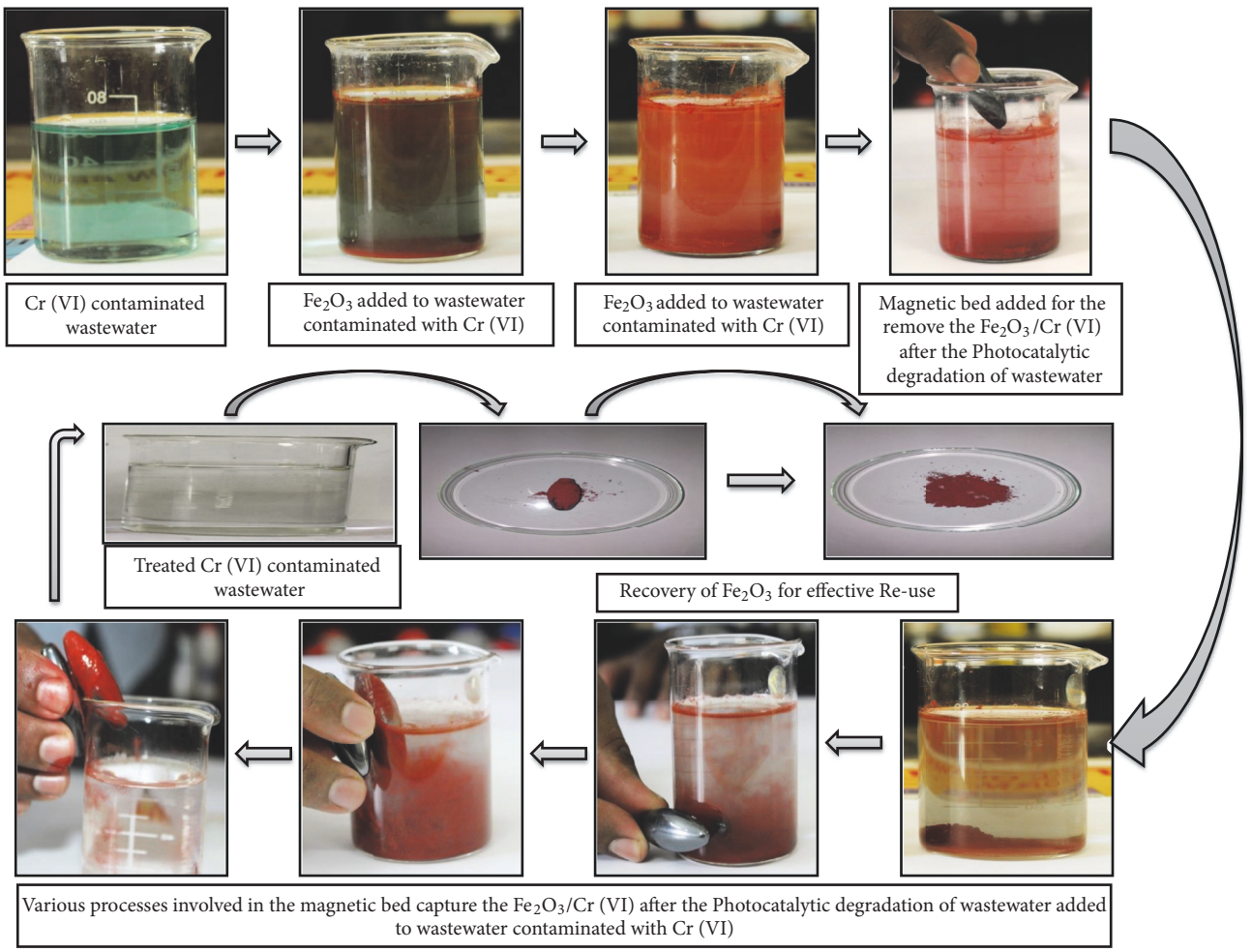

Figure 19: Overall process in removal of Cr(VI) effectively by using Fe_2O_3 nanoporous material.

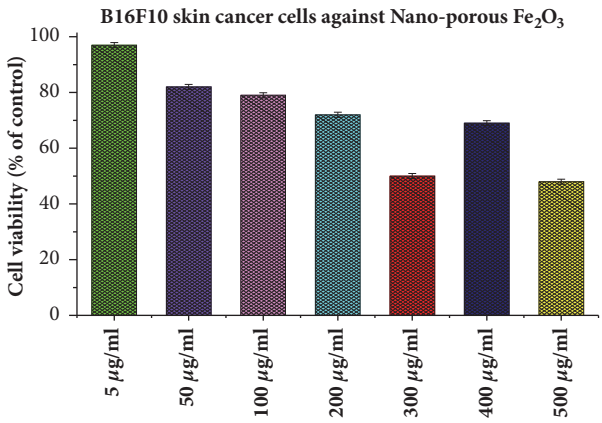

FIGURE 20: Toxicity testing of the Fe_2O_3 nanoporous material using *Mus musculus* skin melanoma cells using various concentrations.

used in the assay did not reduce the cell viability noticeably as compared to other increased concentrations. Among Fe_2O_3 found to be low in systematic manner, nanoporous Fe_2O_3 is the safest and the superlative alternative in terms of toxicity.

4. Conclusion

In summary, we have demonstrated a low-cost hydrothermal method for the preparation of a visible light responsive and magnetically discrete Fe_2O_3. In such an easy process, the preparation procedure is simplified effectively, and the preparation time has been shortened which is beneficial for industrial production. The Fe_2O_3 nanocomposite exhibits the highest photocatalytic activity within 120 min of Cr(VI) and is degraded using 0.75 g L^{-1} of Fe_2O_3, The electron-hole separation process in the nanocomposite has also been explained schematically. The high recyclability of Fe_2O_3 nanoporous material is expected to have excellent application prospects as a good photocatalyst in wastewater treatment, which needs further investigation. Moreover, the synthesized samples are highly stable in the photocatalytic process and nontoxic to the living cells. Hence, the combination of high photocatalytic stability, nontoxicity, and efficient upconversion properties in the synthesized material paves the mode for its application in photocatalysis, energy renovation, and the biological area.

Data Availability

The data used to support the findings of this study are available from the corresponding author upon request.

Conflicts of Interest

The authors declare that there are no conflicts of interest regarding this manuscript.

Acknowledgments

The first author Abhilash M. R. (IF160104) is thankful to the Department of Science and Technology, Govt. of India, New Delhi, for awarding the financial assistance through DST-*INSPIRE* Junior Research Fellowship to carry-out the research in the University of Mysore, Mysuru 570 006, Karnataka, India.

Supplementary Materials

Overall process involved in visible light assisted photocatalytic degradation of chromium (VI) by using nanoporous Fe_2O_3. *(Supplementary Materials)*

References

[1] D. S. Bhatkhande, V. G. Pangarkar, and A. A. Beenackers, "Photocatalytic degradation for environmental applications—a review," *Journal of Chemical Technology and Biotechnology*, vol. 77, no. 1, pp. 102–116, 2002.

[2] A. Mills, A. Belghazi, and D. Rodman, "Bromate removal from drinking water by semiconductor photocatalysis," *Water Research*, vol. 30, no. 9, pp. 1973–1978, 1996.

[3] A. Lozano, J. Garcia, X. Dormènech, and J. Casado, "Heterogeneous photocatalytic oxidation of manganese(II) over TiO2," *Journal of Photochemistry and Photobiology A: Chemistry*, vol. 69, no. 2, pp. 237–240, 1992.

[4] P. Suksabye, P. Thiravetyan, W. Nakbanpote, and S. Chayabutra, "Chromium removal from electroplating wastewater by coir pith," *Journal of Hazardous Materials*, vol. 141, no. 3, pp. 637–644, 2007.

[5] Z. Kowalski, "Treatment of chromium tannery wastes," *Journal of Hazardous Materials*, vol. 37, no. 1, pp. 137–144, 1994.

[6] J. Giménez, M. Aguado, and S. Cervera-March, "Photocatalytic reduction of chromium(VI) with titania powders in a flow system Kinetics and catalyst activity," *Journal of Molecular Catalysis A: Chemical*, vol. 105, no. 1-2, pp. 67–78, 1996.

[7] M. A. Barkat, Y. T Chen, and C. P Huang, "Removal of toxic cyanide and Cu(II) ion from water illuminated TiO_2 catalyst," *Applied Catalysis B: Environmental*, vol. 53, no. 1, pp. 13–20, 2004.

[8] V. Sarin and K. K. Pant, "Removal of chromium from industrial waste by using eucalyptus bark," *Bioresource Technology*, vol. 97, no. 1, pp. 15–20, 2006.

[9] F. N. Acer and E. Malkoc, "The removal of chromium (VI) from aqueous solution by Fagus Orientals L," *Bioresource Technology*, vol. 94, no. 1, pp. 13–15, 2004.

[10] P. Kajitvichyanukul, J. Ananpattarachai, and S. Pongpom, " Sol–gel preparation and properties study of TiO ," *Science and Technology of Advanced Materials*, vol. 6, no. 3-4, pp. 352–358, 2005.

[11] S. K. Srivastava, V. K. Gupta, and D. Mohan, "Kinetic parameters for the removal of lead and chromium from wastewater using activated carbon developed from fertilizer waste material," *Environmental Modeling & Assessment*, vol. 1, no. 4, pp. 281–290, 1996.

[12] K. Kabra, R. Chaudhary, and R. Sawhney, "Solar photocatalytic removal of Cu(II), Ni(II), Zn(II) and Pb(II): Speciation modeling of metal–citric acid complexes," *Journal of Hazardous Materials*, vol. 155, no. 3, pp. 424–432, 2008.

[13] E. C. Butler and A. P. Davis, "Photo-catalytic oxidation in aqueous titanium dioxide suspension: the influence of dissolved transition metals," *Journal of Photochemistry and Photobiology A: Chemistry*, vol. 70, no. 3, pp. 273–283, 1993.

[14] W.-Y. Lin, C. Wei, and K. Rajeshwar, "Photocatalytic Reduction and Immobilization of Hexavalent Chromium at Titanium Dioxide in Aqueous Basic Media," *Journal of The Electrochemical Society*, vol. 140, no. 9, pp. 2477–2482, 1993.

[15] K. Lee, N. Lee, S. Shin, H. Lee, and S. Kim, "Hydrothermal synthesis and photocatalytic characterizations of transition metals doped nano TiO2 sols," *Materials Science and Engineering: B*, vol. 129, no. 1-3, pp. 109–115, 2006.

[16] C. R. Chenthamarakshan, K. Rajeshwar, and E. J. Wolfrum, "Heterogeneous photocatalytic reduction of Cr(VI) in UV-irradiated titania suspensions: effect of protons, ammonium ions, and other interfacial aspects," *Langmuir*, vol. 16, no. 6, pp. 2715–2721, 2000.

[17] S. Wang, "A Comparative study of Fenton and Fenton-like reaction kinetics in decolourisation of wastewater," *Dyes and Pigments*, vol. 76, no. 3, pp. 714–720, 2008.

[18] H. Tang, F. Lévy, H. Berger, and P. E. Schmid, "Urbach tail of anatase TiO2," *Physical Review B: Condensed Matter and Materials Physics*, vol. 52, no. 11, pp. 7771–7774, 1995.

[19] J. Chang, Q. Ma, J. Ma, and H. Ma, "Synthesis of Fe3O4 nanowire@CeO2/Ag nanocomposites with enhanced photocatalytic activity under sunlight exposure," *Ceramics International*, vol. 42, no. 10, pp. 11827–11837, 2016.

[20] F. Chen, F. Yan, Q. Chen et al., "Fabrication of Fe3O4@SiO2@TiO2 nanoparticles supported by graphene oxide sheets for the repeated adsorption and photocatalytic degradation of rhodamine B under UV irradiation," *Dalton Transactions*, vol. 43, no. 36, pp. 13537–13544, 2014.

[21] Y. Cao, C. Li, J. Li, Q. Li, and J. Yang, "Magnetically Separable Fe3O4/AgBr Hybrid Materials: Highly Efficient Photocatalytic Activity and Good Stability," *Nanoscale Research Letters*, vol. 10, no. 1, 2015.

[22] M. Shekofteh-Gohari and A. Habibi-Yangjeh, "Fabrication of novel magnetically separable visible-light-driven photocatalysts through photosensitization of Fe3O4/ZnO with CuWO4," *Journal of Industrial and Engineering Chemistry*, vol. 44, pp. 174–184, 2016.

[23] Z.-P. Li, Y.-Q. Wen, J.-P. Shang, M.-X. Wu, L.-F. Wang, and Y. Guo, "Magnetically recoverable Cu2O/Fe3O4 composite photocatalysts: Fabrication and photocatalytic activity," *Chinese Chemical Letters*, vol. 25, no. 2, pp. 287–291, 2014.

[24] K. M. Joshi and V. S. Shrivastava, "Photocatalytic degradation of Chromium (VI) from wastewater using nanomaterials like TiO2, ZnO, and CdS," *Applied Nanoscience*, vol. 1, no. 3, pp. 147–155, 2011.

[25] R. Satheesh, K. Vignesh, A. Suganthi, and M. Rajarajan, "Visible light responsive photocatalytic applications of transition metal (M = Cu, Ni and Co) doped α-Fe2O3 nanoparticles," *Journal of Environmental Chemical Engineering (JECE)*, vol. 2, no. 4, pp. 1956–1968, 2014.

[26] L. J. Sanches, P. C. Marinello, C. Panis et al., "Cytotoxicity of citral against melanoma cells: The involvement of oxidative stress generation and cell growth protein reduction," *Tumor Biology*, vol. 39, no. 3, 2017.

[27] P. Kumar, C. Joshi, A. Barras et al., "Core–shell structured reduced graphene oxide wrapped magnetically separable rGO@CuZnO@Fe3O4 microspheres as superior photocatalyst for CO2 reduction under visible light," *Applied Catalysis B: Environmental*, vol. 205, pp. 654–665, 2017.

[28] A. Kumar, Shalini, G. Sharma et al., "Facile hetero-assembly of superparamagnetic Fe3O4/BiVO4 stacked on biochar for solar photo-degradation of methyl paraben and pesticide removal from soil," *Journal of Photochemistry and Photobiology A: Chemistry*, vol. 337, pp. 118–131, 2017.

[29] K. S. Sing, "Reporting physisorption data for gas/solid systems with special reference to the determination of surface area and porosity (Recommendations 1984)," *Pure and Applied Chemistry*, vol. 57, no. 4, pp. 603–619, 1985.

[30] J. Zhang, Y. Wang, J. Jin, Z. Lin, F. Huang, and J. Yu, "Efficient visible-light photocatalytic hydrogen evolution and enhanced photostability of core/shell CdS/g-C_3N_4 nanowires," *ACS Applied Materials & Interfaces*, vol. 5, no. 20, pp. 10317–10324, 2013.

[31] H. Chen and Y. Xu, "Photoactivity and stability of Ag2WO4for organic degradation inaqueous suspensions," *Applied Surface Science*, vol. 319, no. 1, pp. 319–323, 2014.

[32] B. Zhu, P. Xia, Y. Li, W. Ho, and J. Yu, "Fabrication and photocatalytic activity enhanced mechanism of direct Z-scheme g-C3N4/Ag2WO4 photocatalys," *Applied Surface Science*, vol. 391, no. 1, pp. 175–183, 2017.

[33] C. R. Keenan and D. L. Sedlak, "Factors Affecting the Yield of Oxidants from the Reaction of Nanoparticulate Zero-Valent Iron and Oxygen," *Environmental Science & Technology*, vol. 42, no. 4, pp. 1262–1267, 2008.

[34] G. Wojciechowski and B. Brzezinski, "Formation of hydrogen-bonded chains through inter- and intra-molecular hydrogen bonds by 5,5′-dinitro-2,2′-biphenol with a strong base of guanidine-like character and triethylamine," *Journal of Molecular Structure*, vol. 607, no. 2-3, pp. 149–154, 2002.

[35] G. Wojciechowski and B. Brzezinski, "Formation of hydrogen-bonded complexes of 3,3′,5,5′-tetrabromo-2,2′-biphenol with MTBD and triethylamine," *Journal of Molecular Structure*, vol. 616, no. 1-3, pp. 67–71, 2002.

[36] Y. Hou, Z. Xu, and S. Sun, "Controlled synthesis and chemical conversions of FeO nanoparticles," *Angewandte Chemie International Edition*, vol. 46, no. 33, pp. 6329–6332, 2007.

[37] G. Liu, S. Liu, Q. Lu, H. Sun, F. Xu, and G. Zhao, "Synthesis of monoclinic BiVO4 microribbons by sol-gel combined with electrospinning process and photocatalytic degradation performances," *Journal of Sol-Gel Science and Technology*, vol. 70, no. 1, pp. 24–32, 2014.

[38] B. Halliwell and J. M. C. Gutteridge, "Biologically relevant metal ion-dependent hydroxyl radical generation. An update," *FEBS Letters*, vol. 307, no. 1, pp. 108–112, 1992.

[39] M. Yin, Z. Li, J. Kou, and Z. Zou, "Mechanism investigation of visible light-induced degradation in a heterogeneous TiO2/eosin Y/rhodamine B system," *Environmental Science & Technology*, vol. 43, no. 21, pp. 8361–8366, 2009.

[40] M. R. Sohrabi and M. Ghavami, "Photocatalytic degradation of Direct Red 23 dye using UV/TiO2: Effect of operational parameters," *Journal of Hazardous Materials*, vol. 153, no. 3, pp. 1235–1239, 2008.

[41] X. van Doorslaer, P. M. Heynderickx, K. Demeestere, K. Debevere, H. van Langenhove, and J. Dewulf, "TiO_2 mediated heterogeneous photocatalytic degradation of moxifloxacin: operational variables and scavenger study," *Applied Catalysis B: Environmental*, vol. 111-112, pp. 150–156, 2012.

[42] Y. Yamada, A. Nomura, H. Tadokoro, and S. Fukuzumi, "A composite photocatalyst of an organic electron donor–acceptor dyad and a Pt catalyst supported on semiconductor nanosheets for efficient hydrogen evolution from oxalic acid," *Catalysis Science & Technology*, vol. 5, no. 1, pp. 428–437, 2015.

[43] M. Butler and D. Ginley, "Predictions of flatband potentials at semi-conductor interfaces from atomic electronegatives," *Journal of The Electrochemical Society*, vol. 125, no. 1, pp. 228–232, 1978.

[44] Q. Liang, L. Yu, W. Jiang, S. Zhou, S. Zhong, and W. Jiang, "One-pot synthesis of magnetic graphitic carbon nitride photocatalyst with synergistic catalytic performance under visible-light irradiation," *Journal of Photochemistry and Photobiology A: Chemistry*, vol. 335, pp. 165–173, 2017.

[45] S. Thangavel, S. Thangavel, N. Raghavan, R. Alagu, and G. Venugopal, "Efficient visible-light photocatalytic and enhanced photocorrosion inhibition of Ag2WO4 decorated MoS2 nanosheets," *Journal of Physics and Chemistry of Solids*, vol. 110, pp. 266–273, 2017.

[46] Y. V. De Santana, J. E. Gomes, L. Matos et al., "Silver Molybdate and Silver Tungstate Nanocomposites with Enhanced Photoluminescence," *Nanomaterials and Nanotechnology*, vol. 4, p. 22, 2014.

[47] S. Zhang, X. Zhao, H. Niu, Y. Shi, Y. Cai, and G. Jiang, "Superparamagnetic Fe3O4 nanoparticles as catalysts for the catalytic oxidation of phenolic and aniline compounds," *Journal of Hazardous Materials*, vol. 167, no. 1-3, pp. 560–566, 2009.

[48] N. Ferroudj, J. Nzimoto, A. Davidson et al., "Maghemite nanoparticles and maghemite/silica nanocomposite microspheres as magnetic Fenton catalysts for the removal of water pollutants," *Applied Catalysis B: Environmental*, vol. 136-137, pp. 9–18, 2013.